Open access • Journal Article • DOI:10.1063/1.370809

Accurate method for determining adhesion of cantilever beams — Source link

M. P. de Boer, Terry A. Michalske

Published on: 29 Jun 1999 - Journal of Applied Physics (American Institute of Physics)

Topics: Cantilever, Beam (structure) and Surface micromachining

SAND99-0055J
Paper submitted to J. Appl. Phys.

Accurate method for determining adhesion of cantilever beams

M. P. de Boer[1] and T. A. Michalske[2]

Sandia National Laboratories

[1]Intelligent Micromachining, Dept. 1725, MS 1080, Albuquerque, NM 87185,
email: mpdebo@sandia.gov, web page:*www.mdl.gov/Micromachine*

[2]Surface and Interface Science, Dept. 1114, MS 1413, Albuquerque, NM 87185
email: tamicha@sandia.gov

Abstract

Using surface micromachined samples, we demonstrate the accurate measurement of cantilever beam adhesion by using test structures which are adhered over long attachment lengths. We show that this configuration has a deep energy well, such that a fracture equilibrium is easily reached. When compared to the commonly used method of determining the shortest attached beam, the present method is much less sensitive to variations in surface topography or to details of capillary drying.

DISCLAIMER

DISCLAIMER

Portions of this document may be illegible in electronic image products. Images are produced from the best available original document.

1. Introduction

Microelectromechanical Systems or MEMS [1] are now being used in selected commercial products including airbag accelerometers for automobiles [2] and active optical elements [3] for projection displays. Due to their potential for low cost manufacturing, many other microdevice designs and applications are currently being developed. Microrelays [4], gyros [5], optical switches [6] and security devices [7] are just a few examples. However, auto-adhesion, or spontaneous sticking between MEMS structures, remains a major limitation in bringing this new class of engineering devices to the broader market. MEMS are particularly susceptible to auto-adhesion because the structural members: (1) are constructed in close proximity to each other (within several μms), (2) are highly compliant due to their extreme length to thickness aspect ratio and, (3) have large surface to volume ratios which increase the relative importance of adhesive surface forces. If the miniature structural members are brought together by surface (capillary, electrostatic) or inertial (shock, rapid air flow) forces, they may remain adhered after the external force is removed. Auto-adhesion can lead to catastrophic failure of a MEMS device.

From a practical point of view, auto-adhesion is known to limit manufacturing yield of silicon-based, surface micromachined MEMS. In these devices, structural members are fabricated using successively patterned depositions of thin film polycrystalline silicon (polysilicon) and sacrificial oxide layers. This manufacturing approach is a direct outgrowth of silicon-based microelectronics. Auto-adhesion can occur during the final step of surface micromachine fabrication after the polysilicon structural elements are rendered mechanically free by selectively etching away the sacrificial oxide layers in a hydrofluoric acid solution, which does not dissolve the polysilicon. During the final stage of drying from the wet etch, capillary menisci form between the released beams and the substrate and can generate forces that collapse the structural member onto the substrate. Subsequently, the polysilicon material may remain adhered to the substrate after the water dries. The problem is also commonly referred to as "stiction". Numerous efforts have been directed at measuring autoadhesion and correlating to chemistry or roughness of the interface [8-19]. A supercritical drying procedure can be used to eliminate capillary forces during drying and prevent surfaces from coming into contact initially [20]. However, this approach does not address autoadhesion of surfaces that come into contact while devices are in operation. Many coating processes aimed at reducing the surface energy of polysilicon have also been explored [8, 21-23]. Even though some of these coating strategies, particularly those based on silane coupling agents, have shown some promise for improving manufacturing yield and MEMS performance, their optimization requires a quantitative approach for measuring surface energy directly on micromachined devices. The interacting effects of coating material, roughness and environmental aging on adhesion and friction must be understood in order to guarantee that the effect of surfaces

forces on performance and reliability of micromachines will allow proper operation of devices over their lifetimes.

A theory and experimental method for measuring surface energy of micromachined cantilever beams has been proposed by Mastrangelo and Hsu [10-12]. They model the role of capillary forces in bringing beams into contact with the substrate and determine critical beam lengths for beam collapse [11]. As drying continues, the capillary volume diminishes leaving only surface driven interfacial adhesion. Adhesion of the dried cantilever beam is predicted by considering the elastic energy in the deformed beam, which is attempting to pull the beam up off the substrate, and the surface energy that is promoting continued adhesion. By considering these two factors, Mastrangelo and Hsu calculated peel bounds [12] and the adhered length in the limit where the capillary volume vanishes.

Mastrangelo and Hsu [10] (we will subsequently refer to this paper as M&H) predict two configurations in which auto-adhered cantilever beams may be found. Long beams are adhered over a large fraction of their length, and bend into an S-shape as in Fig 1a. Here, the support post is at a height h. The distance from the support post to the point at which the beam comes into contact with the substrate is s, and the length of the beam L is significantly greater than s. In this paper, we assume a fracture mechanics formalism [24] , and call s the crack length. Alternatively, short adhered beams contact the substrate only at their tip, and the beams assume an arc-shaped deformation as in Fig.1b. In this case, the crack length s is very nearly equal to L.

M&H argue that either adhesion geometry can be used to extract a quantitative measure of micromachine surface energy. For S-shaped beams, the crack length s can be used to determine the apparent surface energy. However, an out-of-plane measurement technique is required to determine s. Because such a method is not commonly available in laboratories, M&H recommend using the arc-shaped beam. Then, using a high power objective on an optical microscope, adhesion energy is determined by observing the shortest beam to remain adhered within an array of beams of various lengths. M&H demonstrated the shortest adhered beam approach on polysilicon micromachined beams having both hydrophilic and hydrophobic nature. Although their measurements yield surface energy of reasonable magnitude, they were not able to distinguish between hydrophilic and hydrophobic surfaces.

In this paper, we examine the adhesion measurement approach proposed by M&H in detail. Using interferometry to measure beam deformations point by point, we extend the experimental measurement to include adhesion of S-shaped beams. By taking this approach we directly address the following outstanding questions:

(1) Do the deformations predicted by M&H, which are subsequently used to calculate strain energy, match actual beam deflections?

(2) What is the behavior of beams in the transition region between these two regimes? How are the equilibria for the S-shaped and arc-shaped beams attained?

(3) Are the values for adhesion between S-shaped and arc-shaped beams equivalent? If not, what factors influence measured differences?.

II. Adhesion and Surface Energy of Cantilever Beams

A) Beam Deformations

The total energy of the adhered beam is a sum of (a) the elastic energy stored by bending a beam into contact with the substrate, and (b) the surface energy reduction achieved by forming a beam/substrate interface. Solving for the minimum total energy system allows one to directly determine the equilibrium surface energy. The first step in this approach is a quantitative evaluation of the stored elastic energy in an adhered beam.

In the absence of externally applied forces, the deformations for an adhered beam are given by M&H as

$$u(\eta) = h\eta^2 \left[(m(s)-2)\eta + (3-m(s))\right] \quad , \quad \eta = \frac{x}{s}, \tag{1}$$

where h is the height of the support post, t is the thickness of the beam, L is the beam length and s is the non-adhered length (see Fig. 1). The attachment length d is the length along which the two materials are in contact, and $d \approx L - s$. The slope parameter m is defined by $\theta = m(h/s)$, where θ is the shear angle of the beam tip. From M&H, the functional form of m is

$$m(s) = \frac{\frac{16}{5}\left(\frac{t}{d}\right)^3\left(\frac{t}{s}\right)\left[1+\frac{15}{32}\left(\frac{d}{t}\right)^2\left(\frac{E}{G_s}\right)\right]}{1+\frac{32}{15}\left(\frac{t}{d}\right)^3\left(\frac{t}{s}\right)\left[1+\frac{15}{32}\left(\frac{d}{t}\right)^2\left(\frac{E}{G_s}\right)\right]}, \tag{2}$$

where G_s is the shear modulus. $E/G_s = 2(1+\upsilon) \approx 2.44$ where $\upsilon = 0.22$ is Poisson's ratio for silicon.

For the S-shaped beam, $d >> t$. Consequently, m approaches zero implying no shear deformations at the end of the beam. In the limit when s approaches L, m is a strong function of d, reaching a maximum value of 3/2 for vanishing d. The non-zero slope parameter corresponds to shear deformations induced when adhesive contact is localized to the beam tip.

The assumptions in the M&H analysis are (1) small deformations such that linear elasticity applies, (2) a rigid cantilever support post and substrate, (3) free slip of the beam over the

substrate, (4) attractive forces that operate only between contacting portions of the beam and substrate surfaces, (5) no residual strain (curvature) in the beam, and (6) perfectly smooth beam and substrate surfaces.

B) Equilibrium

In this section, we extend the analysis of M&H to investigate the mechanical equilibria of the S-shaped and arc-shaped cases. We shall find that the energy well is much deeper for the S-shaped than the arc-shaped deformation and that m can *only* take on values near 0 or near 3/2.

Using the deformation characteristics from the previous section, the elastic strain energy in an adhered beam is given by

$$U_E = \frac{EI}{2}\int_0^s \left(\frac{d^2u}{dx^2}\right)^2 dx = \frac{6EIh^2}{s^3}\left(1 - m(s) + \frac{m^2(s)}{3}\right) \tag{3}$$

where $I = wt^3/12$ is the beam moment of inertia, and E is its Young's modulus. Eq. (2) shows that as the crack length s decreases, the stored elastic energy increases. The surface energy U_s is

$$U_s = -\Gamma w(L-s) \tag{4}$$

where Γ is the energy of adhesion per unit area. The surface energy term is negative because energy is reduced when surfaces come into contact. For clean smooth surfaces which are reversibly separated, we expect the adhesion $\Gamma = 2\gamma$, where γ is the surface energy of the material in question. Because the beam and substrate are made of the same material, no separate interfacial energy exists and the adhesion energy Γ is simply twice the surface energy. In actual micromachined beams, factors such as surface roughness and capillary condensation must be considered when evaluating the effective surface energy.

The total system energy U_T is the sum of the elastic strain energy and the adhesive surface energy:

$$U_T = U_E + U_S = \frac{6EIwh^2}{s^3}\left(1 - m(s) + \frac{m^2(s)}{3}\right) - \Gamma w(L-s) \tag{5}$$

System equibrium is determined by stable values of U_T defined by

$$\frac{dU_T}{ds} = 0 \tag{6a},$$

and $$\frac{d^2U_T}{ds^2} > 0 \tag{6b}$$

To characterize the system equilibrium, we determine stable values of U_T for various length beams assuming a fixed value of Γ. A straightfoward method to solving Eq. (6) is by the graphical method. It is necessary to eliminate d from Eq. (2) using $d \approx L - s$. Then, Eq. (2) can be rewritten as

$$m(s) = \frac{A(s)}{1 + (2/3)\,A(s)}, \tag{7}$$

where $A(s)$ is defined in terms of known constants and variable s as

$$A(s) = \frac{16}{5}\left(\frac{t}{L-s}\right)^3\left(\frac{t}{s}\right)\left[1 + 1.144\left(\frac{L-s}{t}\right)^2\right]. \tag{8}$$

Using (5), (7) and (8), we plot in Fig. 2 U_T vs s for various values of L assuming Γ=3.66 mJ/m^2, t=2.3 μm, h=1.8 μm and w=20 μm (reflecting the data for hydrophobic samples in section III below). The state in which the system will reside is the lowest *reachable* minimum for U_T after drying. In Appendix 1, we estimate two characteristic lengths, $L_{tip,0}$ and $L_{tip,c}$. The former is the minimum length beam which will be brought into contact with the substrate at an angle of 0° at its tip, while the latter is the shortest beam which will be brought into contact at some angle. The reachable minimum, after drying is complete, depends on the shortest value of $s = s_{\min}$ achieved while external forces pull the beam into contact with the substrate. As seen in Appendix 1, this depends on both the surface tension of the liquid as well as its contact angle with the substrate. In this example, we shall take $s_{\min} = L_{tip,0}$=200 μm for S-shaped beams, reflecting a receding contact angle during the drying process of θ_c=80°.

Fig. 2a is a graph of U_T and m vs s for L=400 μm. For small s, U_T grows large due to bending strain energy U_E, while m is near 0. Note that m (plotted on a logarithmic scale) is not exactly 0 because the theory accounts for beam shearing at the crack tip, which exists to a small degree even for the S-shaped beam. For large s, U_T increases because surface energy U_S becomes substantial. However, as $s \to L$, m rapidly begins to increase towards 3/2, reflecting the change from the S-shape to the arc-shape. A commensurate decrease in U_E occurs, and is manifested as a local minimum in U_T. Regarding stability, at s_1^*=229, s_2^*=398.2 and s_3^*=399.76 μm (6a) is satisfied, but (6b) is satisfied only at s_1^*=229 and s_3^*=399.76 μm (s^* refers to the local extrema). The absolute system minimum in U_T of -7pJ is at s_1^*=229 μm with m=0. It is

approached and reached from the left hand side because, before drying, $s_{min} < s_1^*$. The local minimum in U_T at s_3^*=399.76 μm is not reachable. For long beams such as in Fig. 2a, the fracture equilibrium is stable due to the relatively deep well of 8 pJ at s_1^*, and is independent of beam length. Note that if s_{min} were greater than s_1^*, as large as ~390 μm, the same equilibrium would be achieved as the sample dries. Then, the equilibrium is reached from the right, but the same equilibrium is found because of the depth of the energy well around s_1^*.

In Fig. 2b the plot is repeated at L=275 μm, where important details have changed. The value of U_T=2.2 pJ at s_1^* has increased because the relative contribution of the surface energy term $\Gamma w(L - s_1^*)$ has decreased. There are again two values of s^* for which both (6a) and (6b) are satisfied, namely at s_1^*=229 and s_3^*=274.80 μm. The system minimum is now at s_3^*. It is not reachable from s_{min} because of the energy barrier of about 0.8 pJ at s_2^* relative to s_1^*. Therefore, the system remains in the local minimum at s_1^* with m=0 when drying is complete. The energy well at s_1^* is now much more shallow than in Fig. 2a, 0.5 pJ. Yet, if s_{min} were greater than s_1^*, as large as ~270 μm, the same equilibrium would be achieved from the right of s_1^*.

As seen in Fig. 2c, the local minima at s_1^* and s_2^* merge as L decreases to 242.3 μm. Now there are only two values of s which satisfy (12a), namely at $s_{12}^* \approx 233$ μm and s_3^*=242.12 μm. Of these, only the latter value satisfies (12b). The value of $s_{12}^* \approx 233$ μm has increased slightly above the earlier value of s_1^*=229 μm at this transition point because the contribution of surface energy continues to diminish. The system minimum at s_3^* is now reachable, but the value of m changes dramatically from nearly 0 to nearly 3/2. The energy well at s_3^* is now exceedingly shallow, only ~0.01 pJ as can be seen in Fig. 2d.

The disappearance of the stable minimum at s_1^* implies an abrupt transition in m from 0 to 3/2 as L decreases. Physically, it can be related to the high stored strain energy in the S-shaped beam relative to the arc-shaped beam. Alternately, one may consider the free body diagram, as in Fig. 3. To maintain the S-shape, a significant moment must develop at the crack tip. This moment effectively develops due to adhesion over the attachment length d. When d becomes too short, the required moment arm developed over d by the adhesive forces cannot be developed and the beam snaps to the arc-shape.

As L decreases further, the beam no longer comes into contact at a slope of m=0 for $L < L_{tip,0}$=200 μm. As shown in Appendix 1, the tip is still brought into contact for $L >= L_{tip,c}$=115.6 μm. Therefore, the beam remains adhered at its tip with m=3/2 after the capillary dries. However, at L=161.9 μm, the energy well at s_3^* dissapears. Therefore, as the capillary drop at the beam tip dries for L<161.9 μm, the beam should pop off if the adhesion is equivalent for S-shaped and arc-shaped beams.

C) Adhesion

From a fracture mechanics perspective [24], a crack driving force is derived from the strain energy release rate, G, defined as

$$G=-\frac{1}{w}\frac{dU}{ds}. \tag{9}$$

Here, the rate refers to changing values of s. The adhesion is determined when the strain energy release rate, G, equals the crack resistance or adhesion, Γ, i.e.,

$$G=\Gamma. \tag{10}$$

This is identical to the condition (6a) above. Combining (3) and (10) results in

$$G=\frac{E\,t^3h^2}{2}\left\{\left(3s^{-4}\right)\left[\frac{m^2(s)}{3}-m(s)+1\right]+\left(s^{-3}\right)\frac{dm(s)}{ds}\left[\frac{2m(s)}{3}-1\right]\right\}. \tag{11}$$

Knowing E, t, and h, G can in principle be determined for *any* adhered beam by measuring s, m and dm/ds. As seen from the discussion of equilibrium above, m can take on values only very near 0 or very near 3/2. For beams adhered in the S-shape, m is slowly varying and hence dm/ds can be taken to be 0. Regarding beams adhered in the arc-shape, it is difficult to experimentally determine a value for dm/ds. The exception is for the shortest adhered beam in the arc-shape, where again dm/ds is 0. Therefore, practically speaking, an adhesion measurement for arc-shaped beams is only possible for the shortest adhered beam. Hence, the two limiting cases of Fig. 1 give rise to the expressions

$$G=\frac{3}{2}\left(\frac{E\,t^3h^2}{s^4}\right) \text{ for } m=0, \tag{12a}$$

and

$$G=\frac{3}{8}\left(\frac{E\,t^3h^2}{s^4}\right) \text{ for } m=3/2. \tag{12b}$$

Here, (12a) applies to any beam of sufficient length, while (12b) applies only to the shortest adhered beam.

S-shaped beams with long attachment length d are always free to approach the equilibrium adhered state; i.e. subsequent to a perturbation on the system which forces s from its equilibrium

value, s_1^* can be reached whether $s > s_1^*$, or $s < s_1^*$. In fact, the situation for large d is very similar to Obreimhof's early fracture mechanics experiment in which the fracture energy of mica was determined [25] from crack length measurements. Note that the situation for (12b), although most commonly used to report adhesion measurements in micromaching [9, 10, 15-17, 26] or to compare calculations to data [27, 28], is precarious at best. This is because the depth of the energy well, already exceedingly small for the arc-shaped beams, approaches zero for the shortest adhered beam. In other words, the equilibrium for small d is not always accessible; i.e., if s grows to be larger than s_3^*, the beam will pop off and an adhesive equilibrium can no longer be found. It is worthwhile to note that the deflections derived by M&H from beam theory, simplify to the case of point loading when $m \rightarrow 3/2$. We now proceed to the measurement of deformations and equilibrium adhered lengths for a range of cantilever beam geometries.

III. Experimental Methods and Results

A) Specimen Fabrication and Surface Treatment

Our micromachined structures were fabricated with one photolithographic mask level. First, an $h = 1.8$ μm oxide was deposited on single crystal <100> oriented silicon. A $t = 2.3$ μm layer of polysilicon (as measured by a WYKO multi-wavelength interferometer) was deposited at 600 °C and then annealed at 1100 °C to relieve residual stresses. Cantilever beams of 20 μm width were defined in an array of increasing L with increments of 2 μm from 10 to 100 μm, and with increments of 5 μm from 100 to 500 μm. The beam support was defined by making the polysilcon wider in this area. The samples were placed in a controlled time HF acid etch such that the oxide under the beams was removed, but remained under the support posts. The samples were next transferred to deionized water, immersed in hydrogen peroxide to form a thin silica layer, and then transferred back to deionized water.

One set of samples was removed from the water and dried in air for two days or more. We shall refer to these as the hydrophilic samples. The other set was treated with a molecular coating of ODTS (octadecyltrichlorosilane, $CH_3(CH_2)_{17}SiCl_3$). We shall refer to these as the hydrophobic samples. ODTS has been investigated as a promising molecule for minimization of adhesion in MEMS [8, 22, 29, 30]. The head group of the organosilane is hydrolyzable, which facilitates the formation of covalent siloxane bonding to the substrate hydroxyl groups as well as between neighboring silane molecules to form a well attached organosilane layer [31]. Meanwhile, the CH_3 tail groups exposed to the surface exhibit low surface energy (~20 mJ/m^2), and are hydrophobic (contact angle ~110°). Following the recipe prescribed in ref. [22], the specimens were transferred from water to isoproponal to isoctane, a series of solvents for which the next is miscible with the previous. The specimens were next submersed in a 1mM ODTS solution of 4:1 hexadecane:chloroform for 30 minutes, during which the ODTS molecules deposit on the

polysilicon surfaces. The specimens were then transferred back to the solvents in reverse order, and finally removed from water and air dried.

B) Measurement Procedures

To make quantitative measurements of beam deformations and adhered length, we equipped our Leitz Orthoplan optical microscope with a Michelson interferometric attachment and green light monochromator (547 nm as characterized by spectrum photometry). To ensure minimal error due to tilt, background fringes were aligned parallel with the length of the beams using the tilt adjustment of the reference surface. Interference fringe intensity was recorded with a CCD camera and subsequently analyzed using a standard image processing program [32]. Linescan intensities along the length of adhered beams were converted into u-deflection vs. x-position data using a computer program. An absolute deflection accuracy of about 50 nm (across the entire beam), and a relative accuracy (pixels near each other) of about 10 nm resulted. The the spatial resolution of our 20X objective was about 1 micron. Measurements of beam height versus distance along the beam were used to assess the adhered beam length and to provide a direct comparison with beam deflections predicted from elasticity theory.

C) Experimental Results

Measured deformations and adhered length for a hydrophilic beam of length L=365 μm are presented in Fig. 4. Fig. 4a is an optical interferometric image showing three such adhered beams. Intensity versus position data from a linescan taken along the beam designated by a white line in Fig. 4a are plotted in the graph of Fig. 4b (right hand y-axis). The beam comes into contact with the substrate at the point where the linescan flattens out, at x=172.4 μm, (u=1820 nm). From the linescan data, u deformations were computed and are plotted as a solid line referenced to the left-hand axis of Fig. 4b. For comparison, predicted deformations for the extremes of m=0 and m=3/2, using Eq. (1), are also plotted using dashed lines. It is seen that the actual deformations agree well with those predicted for the case m=0, consistent with the S-shaped deformation for beams adhered over a signficant fraction of their length. Using measured values of s_1^*=172.4 μm, h=1820 nm, t=2.3 μm and assuming E=170 GPa [33] an adhesion value of Γ=11.63 mJ/m^2 was calculated using Eq. (12a).

Adhesion measurements on various length beams were made to determine the range over which deformations matched the case m=0. For sufficiently long beams, the agreement was excellent. However, as the beam length approached the value of 175 μm, a transition to the m=3/2 deformation was observed. For beams shorter than 175 μm, the value of m toggled between 0 and 3/2. An example of this behavior is seen in Fig. 5. In the interferometric image of Fig. 3a, the 140 μm long beam designated by the white line has fringes out to its tip, indicating an

arc-shaped beam geometry. Figure 3b shows good agreement with the $m=3/2$ deformation condition. The 145 μm beam, just below the designated beam, does not have fringes out to its tip. The measured deformation on this beam agrees well with the $m=0$ beam deformation. Finally, below 145 μm, all beams remain adhered with an arc-shape.

The shortest values of L for which beams remained adhered is 58 μm. Normally Eq. (12b) is used to quantify Γ for this case. The result is that $\Gamma=212$ mJ/m^2. However, as seen in Fig. 6 (for the case of a 68 μm long beam), the measured deformations lie somewhere betweeen that predicted by the $m=0$ and $m=3/2$ limiting conditions. This change in deformation behavior is due to the compliance of the step-up post, which is expected to be non-negligible for beams below 100 μm in this geometry [34]. Compliance in the step-up post reduces the strain energy that is stored in the beam and hence the calculation for adhesion according to Eq. (12b) requires a correction. Although a much smaller effect, the step-up post compliance is also non-zero for case of S-shaped beams, Fig. 4. In Appendix 2, we use the measured slope at the beginning of the beam and match the actual beam deformations to account for the step up post compliance in both the S-shape and arc-shape cases. The correction decreases Γ from 11.6 to 10.2 mJ/m^2 for the S-shaped beams, and from 212 to 118 mJ/m^2 for the arc-shape beams. Note that adhesion Γ remains a factor of 11 different even after this correction!

A summary of results for untreated beams is plotted versus beam length in Fig. 7a. The left hand axis displays values of Γ while the measured slope parameter is referenced to the right hand axis. For long beams in the $m=0$ condition, the variation in Γ reflects beam-to-beam differences in local adhesion. The average and standard deviation for measured adhesion energies are reported in Table I (row 1). Again, data for beams in the transition region and the shortest beams showing step-up post compliance were not included the adhesion analysis.

Even though our ODTS coated beams had a measured contact angle of about 105°, capillary action from drying was still able to pull beams into contact with the substrate. We are certain attachment occurred during drying because beams were observed under an optical microscope to be free just before removing from water. We believe that this result is explained by the observation that *receding* contacting angles are often observed to be smaller than advancing contact angles, a phenomenon known as contact angle hysteresis [35]. Further confirmation of this stems from an experiment in which we performed video microscopy of drying of previously adhered ODTS beams. This in-situ drying experiment was conducted without interferometry in order to allow sufficient free working distance between the water and the microscope objective. Out-of plane deflections could still be observed because green light is weakly transmitting in polysilicon, giving rise to a weak but observable contrast. Although a drying front of water moving across the surface was observed in one video frame and had disappeared in the next (30 msec later) due to its rapid velocity over the hydrophobic surface, water remained microscopically in the vicinity of the beams

for approximately another second, and clearly pulled the beams further in. ODTS density on the substrate surface is known to be a strong function of deposition conditions [36]. We hypothesize that because the ODTS film did not attain maximum density in our deposition, the adhesion-controlling receding contact angle was less than 90°.

For long ODTS treated beams, we observed again excellent agreement with deformations predicted for the $m=0$ condition yielding an s_1^* of 225 μm. This adhesion length corresponds to an adhesion energy of $\Gamma=3.9$ mJ/m^2 using Eq. (13a). By making a correction similar to that described in Appendix 2, the value is reduced to 3.6 mJ/m^2. The transition from $m=0$ to $m=3/2$ was abrupt at $L=250$ to 245 μm; no toggling between the values of m was apparent. The shortest adhered beam was at $L=120$ μm. In this case, the measured deformation conformed well with the $m=3/2$ condition, indicating that compliance in the step-up post is small. Using Eq. (13b) results in an adhesion value of $\Gamma=12.1$ mJ/m^2. The corrected value accounting for step up post compliance per Appendix 2 reduces Γ to 10.1 mJ/m^2. Note that this value remains approximately 3 times larger than that obtained with beams adhered in the S-shaped geometry. The results are summarized in Fig. 7b, and the average and standard deviation for long beams with $m=0$ is tabulated in Table I (row 2). Note that the average value of Γ is approximately four times lower for the hydrophobic than the hydrophilic beams.

IV. Discussion

In this section we use our experimental results to address each of the questions that we posed in Section I.

1) Are the predicted beam deflections valid for micromachined beams?

Using interferometry, we have carefully compared actual beam deformations against those assumed in the model of M&H. For adhered beams which come into contact with the substrate beyond 120 μm from the support post, we find that the deformations match those of M&H quite well. However, we find that the arc-shaped beams with hydrophilic surfaces yield deformations that are considerably different than predicted by the simple model. The explanation is that the deformation model assumes a rigid support post, while the actual micromachined beams have more complex and compliant support post geometeries. In our processing approach, undercutting of the rigid support post occurs during the release etch and contributes additional compliance to the beam structure. In Appendix 2, we showed how the effect of compliance could be evalutated. Other fabrication approaches for support posts, such as that used by M&H, avoid the undercutting problem but also involve inherently compliant support post structures.

Our results show that support post compliance errors increase as the actual adhesion energy increases. This simply reflects the increased torque generated by a larger adhesive force at the adhered end of the beam. Although support post compliance is most apparent for the shortest

adhered beams, close examination of Figs. 4b and 5b suggests that some support-post compliance may be responsible for the small discrepancy between the measured and predicted deformations in the S-shaped configuration. M&H suggest that the effect of support-post compliance on the measured adhesion energy can be removed by plotting the detachment length as a function of beam dimensions. In order to implement this approach one must independently vary the support post height and and beam thickness. However, the processing modifications needed to independently vary the beam dimensions are difficult to achieve and may themselves lead to intrinsic changes in the curavature of the polysilicon or surface roughness that can also influence the measured adhesion energy. For this reason it is best to directly confirm the nature of deflections of the adhered beams and make corrections which account for the step up post compliance. We have carried out this procedure as outlined in Appendix 2.

2) What is the behavior of beams in the transition region between these two regimes? How are the equilibria for the S-shaped and arc-shaped beams attained?

The equilibrium mechanics in section IIB suggests that there should be an abrupt transition length L_{Tr} at which the transition from S-shaped to arc-shaped beams occurs. The values of L_{Tr} can be determined quantitatively by carrying out the exercize in section IIB, based on knowing the value of Γ for S-shaped beams. For the hydrophilic case, the calculated transition length is at L_{Tr}=174.5 μm, while as shown in section IIB, L_{Tr}=242.3 μm for the hydrophobic case. Fig. 7 confirms that this behavior is observed experimentally, and is in excellent quantitative agreement with the calculations for L_{Tr}. For the hydrophilic films, the transition length occurs from 180 μm to140 μm, while for the hydrophobic beams the transition occurs from 250-245 μm. The larger spread observed experimentally in the hydrophilic case is due to larger local differences in adhesion. Note that the ratio of standard deviation to average adhesion for S-shaped beams, σ/Γ, is 0.45 for the hydrophilic beams versus 0.16 for the hydrophobic beams. Because the ratio approaches one-half, it is not surprising to observe that the transition length varies in the hydrophilic case. Hence, a non-abrupt value of L_{Tr} indicates that adhesion is not well controlled locally.

How are the equilibria for the S-shaped and arc-shaped beams attained? For the hydrophilic case, the shortest beam attached is 58 μm. According to the calculations outlined in Appendix 2, this beam is effectively 73 μm long when the step-up post compliance is considered. Therefore, from Table A1, the receding contact angle θ_{cr} of the drying water must be near 0° in the hydrophilic case, because then $L_{tip,c}$~75 μm. Furthermore, from Table A1, for θ_{cr}=0°, $L_{tip,0}$~130 μm. Recall that L_{Tr}=174.5 μm for this case. We hypothesize the following occurs during the drying process: Long beams with $L > L_{Tr}$ approach equilibrium are pulled in to a value $s_{\min} \sim L_{tip,0}$=130 μm when the capillary exerts its maximum force. Because adhesion energy Γ=10 mJ/m^2 is much smaller than $2\gamma\cos(\theta_{cr})$=146 mJ/m^2, surface energy exerts only a weak

subsequent effect and therefore $s_{\min}$ is only slightly less than $L_{tip,0}$. However, because s_1^*=172.4 μm, the equilibrium is approached from the left as the liquid dries. Intermediate length beams with $L_{Tr} > L > L_{tip,0}$ are also pulled into the S-shape by capillary action. The beam gradually reverts to the arc-shape as the capillary dries, because capillary forces remaining over part of the beam will keep it in contact with the substrate. Finally, for short beams with $L < L_{tip,0}$, the beam never attains the S-shape. These remain adhered at their tip, however, as drying progresses. In effect, any beam which contacts the substrate at its tip remains in contact. This is equivalent to the assertion by Abe and Reed [13]. To confirm this hyphothesis, in-situ drying experiments under interferometric conditions are required.

For the hydrophobic case, from Table A1 θ_{cr} is at most 82°, such that beams of length L=120 μm are pulled into contact with the substrate. Therefore, $L_{tip,0}$~210 μm. Surface energy due to capillary force is now $2\gamma\cos(\theta_{cr})$=20 mJ/m^2. This remains larger than surface energy Γ=3 mJ/m^2, $s_{\min}$ is again only slightly less than $L_{tip,0}$. The drying sequence is qualitiatively similar to the hydrophilic case for the long, medium and short length beams.

3) Are the values for adhesion between S-shaped and arc-shaped beams equivalent? If not, what factors influence measured differences?

Using corrections as outlined in Appendix 2, we were able to directly compare the adhesion energy as determined by the conventional shortest attached beam method and by our adhered length approach. We found a significant discrepancy between the results produced by the two methods, factors of 11 and 3 for the hydrophilic and hydrophobic cases respectively. Therefore, the values measured by the two methods *are not equivalent!* Before we address differences between measurement approaches, it is important to understand the absolute values obtained. For this purpose, we consider the hydrophilic samples that were treated only with hydrogen peroxide before drying from D.I. water. This treatment results in beam and substrate surfaces that are covered by a thin layer of hydrophilic SiO_2. In a previous report [37], we showed that the adhesion energy for silica covered surfaces is dominated by the inherent roughness of the polysilicon. For perfectly smooth, wetted surfaces one predicts and measures [38] an adhesion energy that is twice the surface energy of water (γ_{water}= 73 mJ/m^2), or about 146 mJ/m^2. In the case of rough surfaces, the apparent adhesion can be more than an order of magnitude lower due to the limited area of actual contact between surface asperities. This helps us to understand why Γ is much lower than $2\gamma_{water}$ for the hydrophilic beams. Of course, at saturation humidity conditions liquid is expected to fill the entire region surround individual asperities and lead to adhesion values comparable with smooth surface conditions.

Because surface roughness can play a significant factor in the apparent adhesion energy, one might ask whether the differences observed between measurement techniques may also be due to factors associated with surface roughness. The fact that the actual surface roughness was the

same for all beams argues against this notion. However, the contact geometry is quite different for the S-shaped and arc-shaped beams. S-shaped beams make contact with the substrate over a length that is large compared with the scale of the surface roughness. Such a geometry closely approximates the parallel contact of extended surfaces that has been the topic of previous studies of rough surface contact [39]. When the area of contact is much greater than the scale of roughness, it is appropriate to use a statistically averaged measure of surface topograph. Alternatively, arc-shape beams make contact only over microscopic lengths. As seen in Fig. 2d, a beam which has just made the transition from the S-shaped to the arc-shape is adhered over ~200 nm. However, the shortest arc-shaped beams will be adhered only over a few tens of nanometers according to the M&H calculations. The atomic force microscope linescan in Fig. 8 shows that the period of major asperity peaks on these surfaces is greater (~1 μm) than the predicted length of contact at the tip of the beam. In this situation it is clear that statistical models for true contact area will not be reliable. Given this large difference in contact geometries for the two measurement approaches, it is not hard to believe that the actual contact in the vicinity of the crack tip will also be significantly different for each. This actual contact area cannot be explored through direct measurement techniques. It will be interesting in the future to apply numerical techniques such as those developed by Tian and Bhushan [40, 41] to model the actual area of contact for the two contact geometries. Perhaps such estimates could help quantify the effect of roughness on areal contact.

A second effect that may also contribute to the observed difference between apparent adhesion values is related to the drying process itself. As water evaporates from the contact region of arc-shaped beams, impurities will necessarily concentrate in the capillary drop at the tip of the beam. In the limit as the capillary volume vanishes, impurities or soluability products may actually precipitate and lead to the possible formation of a porous solid network in the vicinity of the tip of the beam. Previous fracture mechanics measurements [42] have shown that precipitation of soluable silicates can support stress across solid silicate interfaces. In this scenario, the effective contact area can become much larger than the calculated value leading to an overestimate of the surface energy. Again, the extremely small contact region in the arc-shaped beam makes this measurement approach very sensitive to the nature and size of the contact region. Alternatively, S-shaped beams with thier extended adhesive interface are expected to be much less sensitive to such effects.

While the S-shaped beam gives a more reliable value of adhesion than the arc-shaped beam, the latter is of great practical significance. This is because the shortest beam to adhere will always limit the use of MEMS devices. Two-dimensional meniscus effects on the sticking of arc-shaped beams were discussed in refs. [13] and [14]. Narrow-width arc-shaped beams are less likely to stick than wide arc-shaped beams possibly due to meniscus effects [43]. More work will be

necessary to elucidate the full three dimensional nature of capillary drying and its interplay with adhesion.

V. Summary and Conclusions

We have explored in detail the deformations and adhesive equilibria of micromachined cantilever beams. Our summary and conclusions follow:

(1) The deformations for adhered beams were measured by interferometry for arc-shaped and S-shaped beams, and found to agree to first order with the elasticity calclulations of M&H. This verifies that for long beams (>120 μm for our geometry), the strain energies calculated by M&H are appropriate in making adhesion calculations. Discrepancies were significant for adhered beam lengths less than 120 μm, and could be explained and modeled by non-zero support post compliance.

(2) An abrupt transition from an S-shaped to an arc-shaped beam as L decreases was predicted theoretically, and observed experimentally. This is explained by the disappearance of a local minimum at s_1^* of total system energy U_T as L is decreased. Excellent agreement between calculations and experiment for the transition length L_{Tr} was obtained by using the value for adhesion Γ for S-shaped beams. This suggests that the value of Γ for S-shaped beams controls the transition length, rather than the value of Γ for arc-shaped beams.

(3) Adhesion can be measured on any beam of sufficient length. A long cantilever beam gives a good fracture mechanics equilibrium. When compared to the method of determining the shortest adhered beam in an array of beams, this allows a much smaller area to be used to obtain adhesion values. Also, adhesion statistics can be obtained by measuring several beams in close proximity. Hence, measuring adhesion on S-shaped beams gives much higher resolution on adhesion than the method of determining the shortest adhered beam.

(4) The apparent adhesion calculated for the shortest arc-shaped beam is greater than the adhesion for S-shaped beams. The probable reason is that the the attachment length d for arc-shaped beams, calculated from beam theory but impossible to confirm experimentally, is incorrect. Due to statistical variations in roughness, the contact area sampled by the crack tip of the arc-shaped beam may be smaller or larger than that sampled by the crack tip of the S-shaped beam. If the beam is dried from a liquid environment in which capillary action has brought it in contact with the substrate, the effective contact area is very likely larger than the calculated value, giving rise to an anomaloulsly high value of adhesion.

We have demonstrated that adhesion measurements from S-shaped should be used for detailed studies of adhesion forces in surface micromachining. This method gives great latitude in measuring adhesion because equilibrium is deep and easily attainable from either side of the

equilibrium. Studies such as the effect of environment on adhesion are readily adapted to this method [37]. Adhesion values are relatively insensitive to local statistical variations in the surface topography. Errors in measurement of the attachment length d induce only a small change from true adhesion values. Finally, although surface micromachined structures were used as test samples, the method is independent of scale.

Acknowledgements

Sandia National Laboratories is a multiprogram laboratory operated by Sandia Corporation, a Lockheed-Martin Company, for the United States Department of Energy under Contract DE-AC04-94AL85000. We thank Peggy Clews and Tom Gugliotta and the entire staff at the Microelectronics Development Laboratory at Sandia National Laboratories for preparing the samples.

References

1. C. H. Mastrangelo and W. C. Tang, *Semiconductor Sensors*, S. M. Sze, Ed., 70 (John Wiley & Sons, New York, 1994).
2. F. Goodenough, Electronic Design, August 8, 1991, pp. 45-56.
3. P. F. Vankessel, L. J. Hornbeck, R. E. Meier and M. R. Douglass, Proc. IEEE **86** (8), 1687 (1998).
4. E. J. J. Kruglick and K. S. J. Pister, Hilton Head '98, Hilton Head Island, SC, USA, June 8-11, 1998, pp. 333-337.
5. J. A. Geen, Hilton Head '98, Hilton Head Island, SC, USA, June 8-11, 1998, pp. 51-54.
6. V. Aksyuk et al., Hilton Head '98, Hilton Head Island, SC, USA, June 8-11, 1998, pp. 79-82.
7. M. S. Rodgers and J. J. Sniegowski, Hilton Head '98, Hilton Head Island, SC, USA, June 8-11, 1998, pp. 144-149.
8. R. L. Alley, G. J. Cuan, R. T. Howe and K. Komvopoulos, Hilton Head , 202 (1992).
9. R. L. Alley, P. Mai, K. Komvopoulos and R. T. Howe, Proc. Int. Conf. Solid-State Sensors & Actuators (Transducers '93) , 288 (1993).
10. C. H. Mastrangelo and C. H. Hsu, Hilton Head , 208 (1992).
11. C. H. Mastrangelo and C. H. Hsu, J. MEMS **2** (1), 33 (1993).
12. C. H. Mastrangelo and C. H. Hsu, J. MEMS **2** (1), 44 (1993).
13. T. Abe, W. C. Messner and M. L. Reed, J. MEMS **4** (2), 66 (1995).
14. T. Abe and M. L. Reed, J. Micromech. Microeng. **6** (2), 213 (1996).
15. R. Legtenberg, J. Elders and M. Elwenspoek, Proc. Int. Conf. Solid-State Sensors & Actuators (Transducers '93) , 298 (1993).
16. M. R. Houston, R. T. Howe and R. Maboudian, J. Appl. Phys. **81** (8), 3474 (1997).
17. Y. Yee, K. Chun and J. D. Lee, Proc. Int. Conf. Solid-State Sensors & Actuators (Transducers '95) , 206 (1995).
18. R. Maboudian and R. T. Howe, J. Vac. Sci. Tech. B **15** (1), 1 (1997).
19. C. H. Mastrangelo, Tribology Letters **3**, 223 (1997).
20. G. T. Mulhern, D. S. Soane and R. T. Howe, Proc. Int. Conf. Solid-State Sensors & Actuators (Transducers '93) , 296 (1993).
21. M. R. Houston, R. T. Howe, K. Komvopoulos and R. Maboudian, Mater. Res. Soc. Proc. **383**, 391 (1995).

22. M. R. Houston, R. Maboudian and R. T. Howe, Hilton Head '96, Hilton Head Island, SC, USA, June 3-6, 1996, pp. 42-47.
23. P. F. Man, B. P. Gogoi and C. H. Mastrangelo, Proc. IEEE MEMS (San Diego) , 55 (1996).
24. H. L. Ewalds and R. J. H. Wanhill, *Fracture Mechanics*, 82-84 (Edward Arnold and Delftse Uitgevers Maatschapij, London, 1991).
25. J. W. Obreimoff, Proc. Roy. Soc. Lond. A. **A127**, 290 (1930).
26. U. Srinivasan, M. R. Houston, R. T. Howe and R. Maboudian, Proc. Int. Conf. Solid-State Sensors & Actuators (Transducers '97) **2**, 1399 (1997).
27. K. Komvopoulos and W. Yan, J. Tribol. **119** (3), 391 (1997). (*Note:* theoretical adhesion calculations in this reference and the next assume that the critical stiffness of arc-shaped beams is determined by a one micron contact zone, while the true zone length is vanishingly small).
28. K. Komvopoulos and W. Yan, J. Tribol. **120** (4), 808 (1998).
29. K. Deng, R. J. Collins, M. Mehregany and C. N. Sukenik, J. Electrochem. Soc. **142** (4), 1278 (1995).
30. U. Srinivasan, M. R. Houston, R. T. Howe and R. Maboudian, J. MEMS **7** (2), 252 (1998).
31. D.L. Angst and G.W. Simmons, Langmuir **7**, 2236 (1991).
32. Analysis performed using the public domain NIH image program, available from the NIH Image Web site (http://rsb.info.nih.gov/nih-image/).
33. W. N. Sharpe, R. Vaidyanathan, B. Yuan, G. Bao and R. L. Edwards, J. Vac. Sci. Tech. B **15** (5), 1599 (1997).
34. Q. Meng, M. Mehregany and R. L. Mullen, J. MEMS **2** (3), 128 (1993).
35. J. Israelachvili, *Intermolecular and Surface Forces*, (Academic Press, New York, 1992).
36. M. E. McGovern, K. M. R. Kallury and M. Thompson, Langmuir **10** (10), 3607 (1994).
37. M. P. de Boer, P. J. Clews, B. K. Smith and T. A. Michalske, Mater. Res. Soc. Proc. **518**, 131 (1998).
38. T. A. Michalske and E. R. Fuller, J. Am. Ceram. Soc. **68** (11), 586 (1985).
39. J. A. Greenwood and J. B. P. Williamson, Proc. Roy. Soc. Lond. A. **295**, 300 (1966).
40. X.F. Tian and B. Bhushan, J. Phys. D. Appl. Phys **29** (1), 163 (1996).
41. X. Tian and B. Bhushan, Journal of Tribology **118**, 33 (1996).
42. B. C. Bunker and T. A. Michalske, in *Fracture Mechanics of Ceramics*, R. C. Bradt, A. G. Evans, D. P. H. Hasselman and F. F. Lange, ed. (Plenum Press, New York, 1986), vol. 8, pp. 391-411.
43. C. J. Kim, J. Y. Kim and B. Sridharan, Sensors and Actuators A **64** (1), 17 (1998).

Appendix 1 Determination of characteristic beam lengths $L_{tip,0}$ and $L_{tip,c}$.

Capillary action exerts negative pressure on a beam as seen in Fig. A1. A complete understanding of the drying problem requires a three dimensional analysis [13] and is beyond the scope of this work. However, a reasonable analysis for chararacteristic beam lengths for the case $w>>h$ from which we can gain some insight into the strength of the capillary liquid is provided in this Appendix.

For a given capillary force, we wish to determine the length of the shortest beam, $L_{tip,0}$, for which the beam tip makes an angle $\theta=0$ at some point during the drying process. For any beam of length greater than $L_{tip,0}$, surface energy will cause the crack length to become shorter than $L_{tip,0}$ during the drying process. Beams shorter than $L_{tip,0}$ cannot reach the S-shape configuration. We need to solve for the beam deflection when the capillary extends from the support post to the tip of the beam. In this situation, the beam is uniformly loaded by a force q, as in Fig. A1. A point reaction P at the beam tip opposes this force, Fig. A1.

From beam theory, the beam is in contact with the substrate if

$$w(L) = \frac{qL^4}{8EI} - \frac{PL^3}{3EI} = h \tag{A1}$$

and is at a an angle $\theta=0$ at its tip if

$$\frac{qL^3}{6EI} - \frac{PL^2}{2EI} = 0 \tag{A2}$$

From (A2), $P = qL/3$, and from (A1), $q = 72hEI/L^4$. Therefore, the shortest beam which will be brought into contact to the substrate with an angle $\theta=0$ at its tip is at

$$L_{tip,0} = \left(\frac{72EIh}{q}\right)^{1/4}. \tag{A3}$$

Likewise, the shortest beam which will be brought into contact at its tip (with an angle $\theta>0$) is at a length $L_{tip,c}$, where

$$L_{tip,c} = \left(\frac{8EIh}{q}\right)^{1/4} \tag{A4}$$

The uniform loading q is calculated from the Laplace pressure $q/w=\gamma/r$, where γ_{water}=73 mN/m, and r is the radius of the drop in Fig. A1. It is a simple geometrical exercise to show that $r=(h/2\cos\theta_{cr})$, where θ_{cr} is the receding contact angle of water with the solid. Therefore, $q=2\gamma\cos\theta_{cr}/h$. Finally,

$$L_{tip,0}=\sqrt{3}\,L_{tip,c}=\left(\frac{E\,t^3\,h^2}{3\,\gamma\cos\theta_{cr}}\right)^{1/4} \tag{A5}$$

In Table A1, we give some calculated lengths for $L_{tip,0}$ and $L_{tip,c}$. The values E=170 GPa, $\gamma=\gamma_{water}$, w=20 μm, h=1.8 μm, and t=2.3 μm are assumed.

The analysis here provides an upper bound for $L_{tip,0}$ and $L_{tip,c}$. In reality, factors such as support post compliance and edge effects (such as the "inside meniscus" [13])will reduce these values somewhat. Considering that in our experiments w=11 h, the effect of the inside meniscus will be small.

Table A1 Values for $L_{tip,c}$ and $L_{tip,0}$ vs θ_{cr}

θ_{cr}	$L_{tip,c}$ (μm)	$L_{tip,0}$ (μm)
0	74.6	129.3
30	77.4	134.0
60	88.8	153.7
80	115.6	200.3
85	137.4	237.9
89	205.3	355.7
89.9	365.1	632.4
89.99	649.3	1124.6

Appendix A2 Correcting the values of Γ for support post compliance.

Knowing the deflections for the beams, we can take into account the compliance of the step-up support post to improve the values of Γ. This is done by relaxing the constraint that the constants of integration used to derive the deflection curve Eq. (1) be zero. In these calculations, the 15 μm length of the support post was taken into account. The fact that this region was approximately twice as wide as the beam was also considered. The non-zero slope of the beam from the edge of the support post was set to the experimental value. Assigning the proper non-zero constants of integration, we matched the experimental deflections to calculated deflections. From this, the strain energy and hence the the corrected values of Γ were determined. The results are given in Table A2. As expected, the values of Γ corrected for the support post compliance are smaller than the uncorrected values. For the arc-shaped beam with the hydrophilic treatment, the correction is approximately a factor of two. However, for the other cases, the correction is 30 per cent or less. This is to be expected considering that only the former deviates significantly from the ideal deflections.

Table A2 - Corrected values of Γ

Treatment	Beam shape	s (μm)	uncorrected Γ(mJ/m^2)	corrected Γ (mJ/m^2)
Hydrophilic	arc	58	202.0	91
	S	172	11.6	9.7
Hydrophobic	arc	120	12.1	9.5
	S	225	3.9	3.6

Table I - Γ for S-shaped beams (m=0)

Treatment	Γ (mJ/m^2)	σ	σ/Γ
Hydrophilic	16.5	8.2	0.5
Hydrophobic	3.4	0.5	0.16

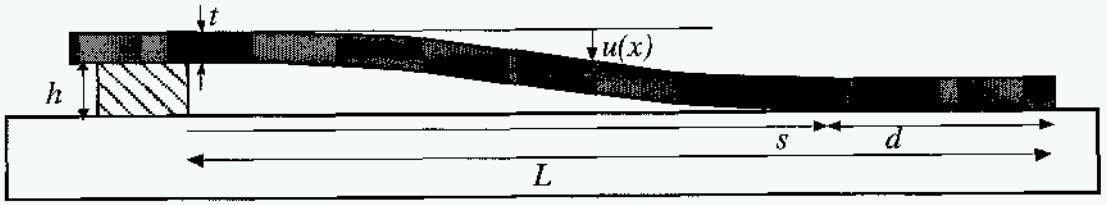

(a) S-shape, (m=0)

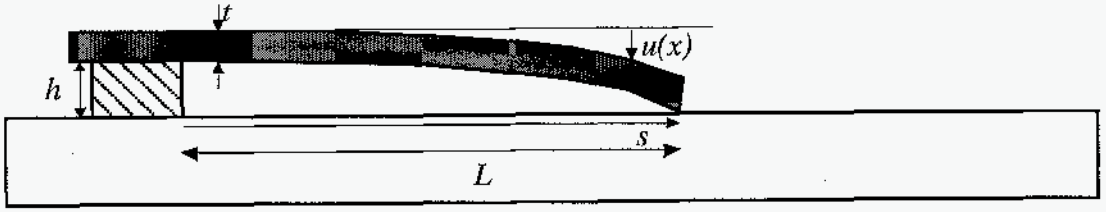

(b) arc-shape, (m=3/2)

Fig. 1

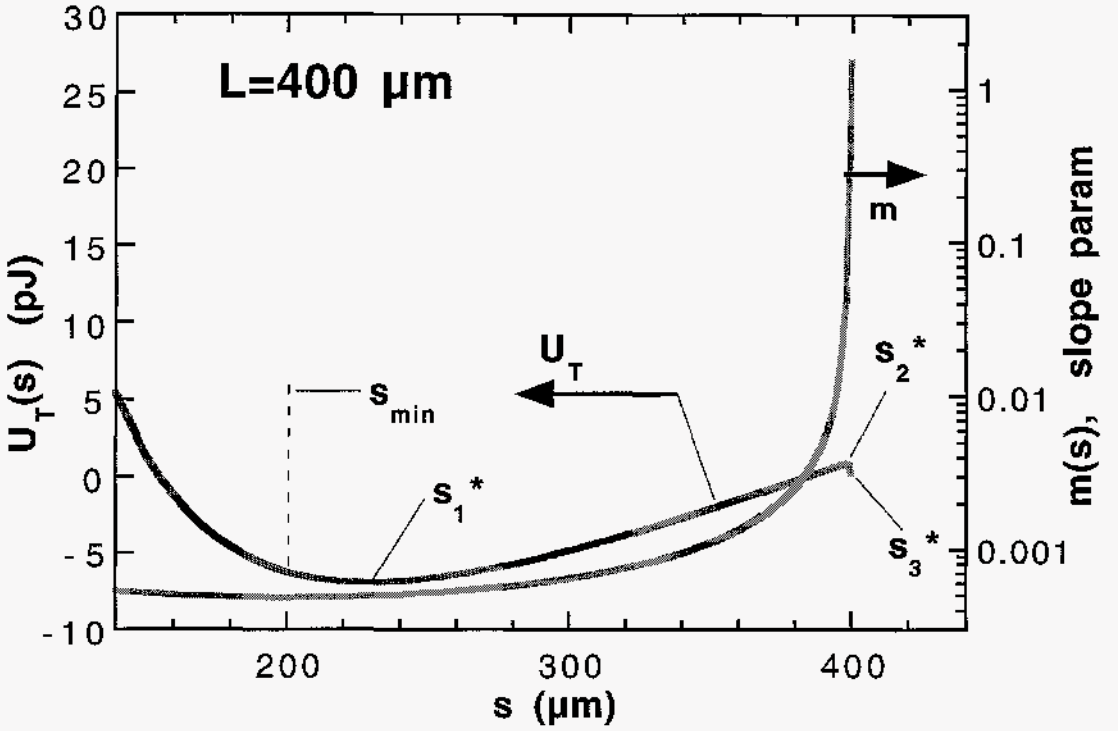
L=400 μm
$U_T(s)$ (pJ)
m(s), slope param
s (μm)
U_T
m
s_{min}
s_1^*
s_2^*
s_3^*
30
25
20
15
10
5
0
- 5
-10
200
300
400
1
0.1
0.01
0.001

Fig. 2a

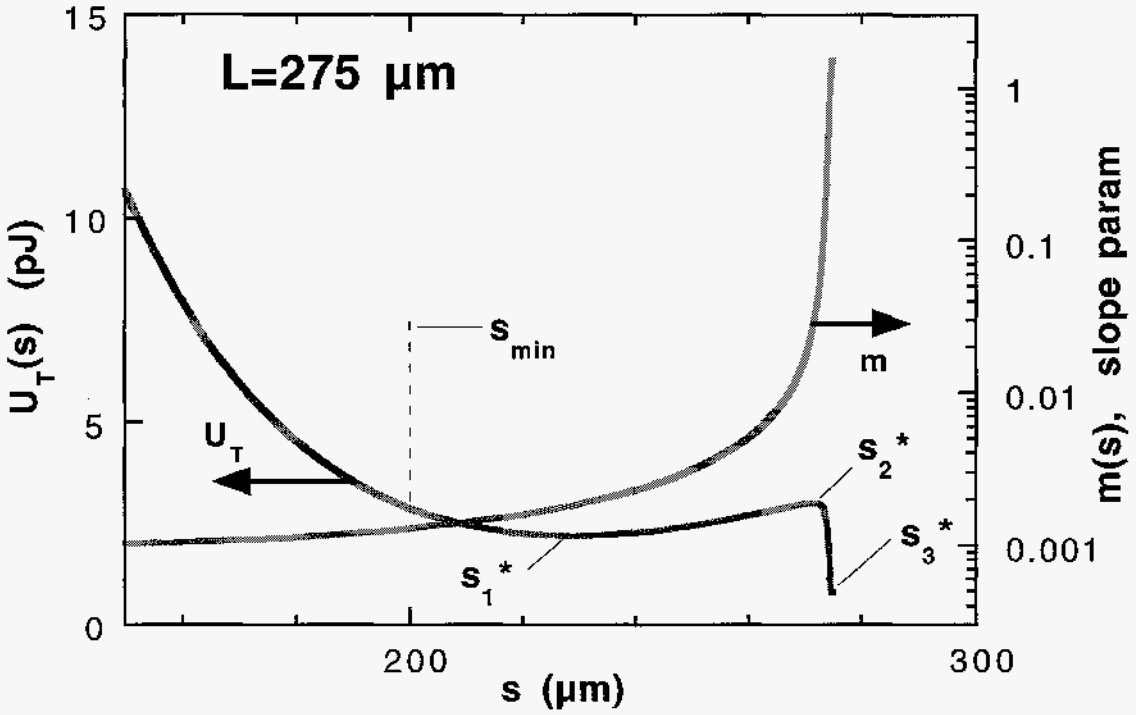
L=275 μm
$U_T(s)$ (pJ)
m(s), slope param
s (μm)
U_T
m
s_{min}
s_1^*
s_2^*
s_3^*
15
10
5
0
200
300
1
0.1
0.01
0.001

Fig. 2b

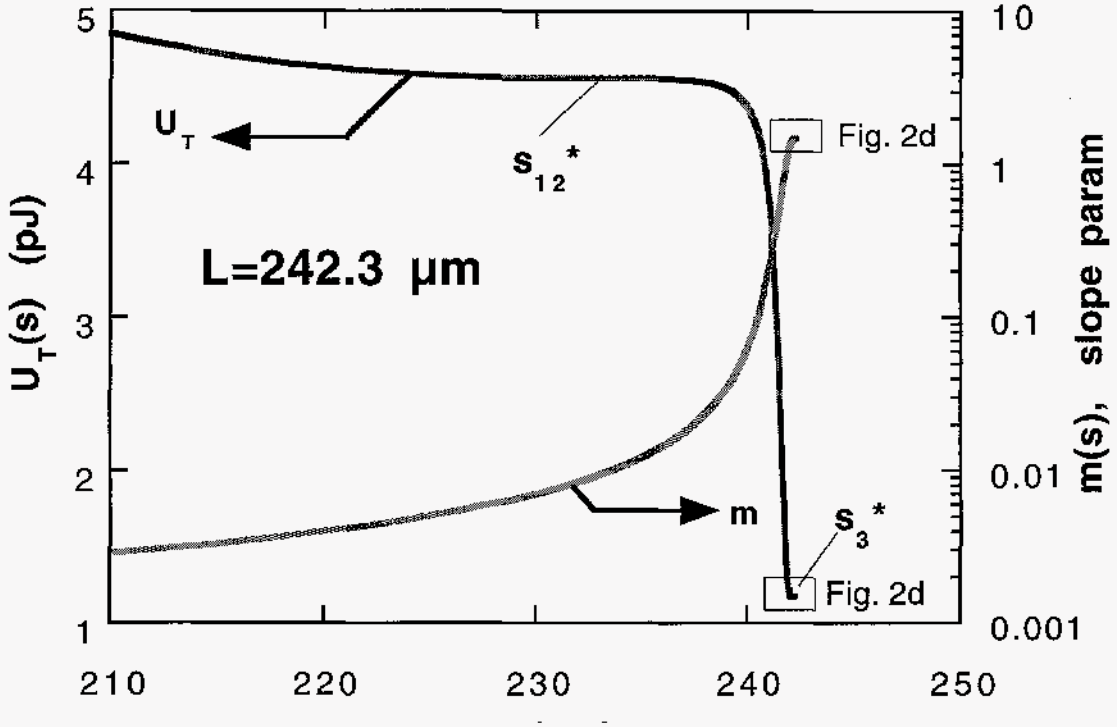
L=242.3 μm
U_T
s_{12}*
s_3*
m
Fig. 2d
Fig. 2d
U_T(s) (pJ)
m(s), slope param
5
4
3
2
1
10
1
0.1
0.01
0.001
210
220
230
240
250

Fig. 2c

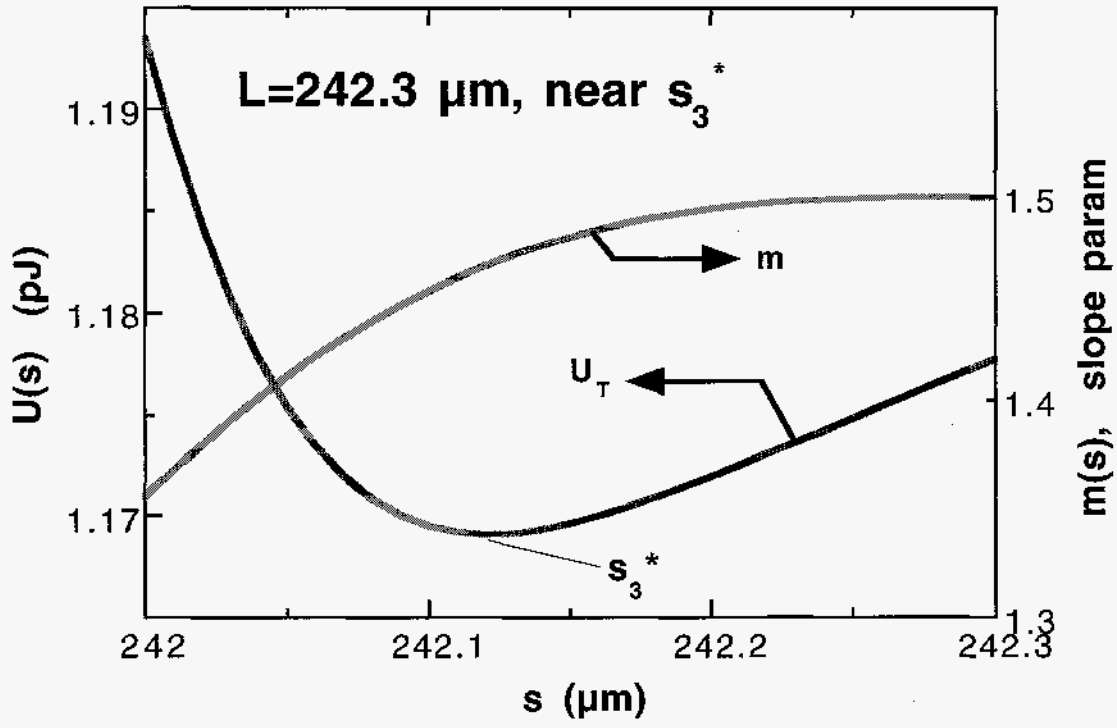
L=242.3 μm, near s_3*
m
U_T
s_3*
U(s) (pJ)
m(s), slope param
1.19
1.18
1.17
1.5
1.4
1.3
242
242.1
242.2
242.3
s (μm)

Fig. 2d

Fig. 3

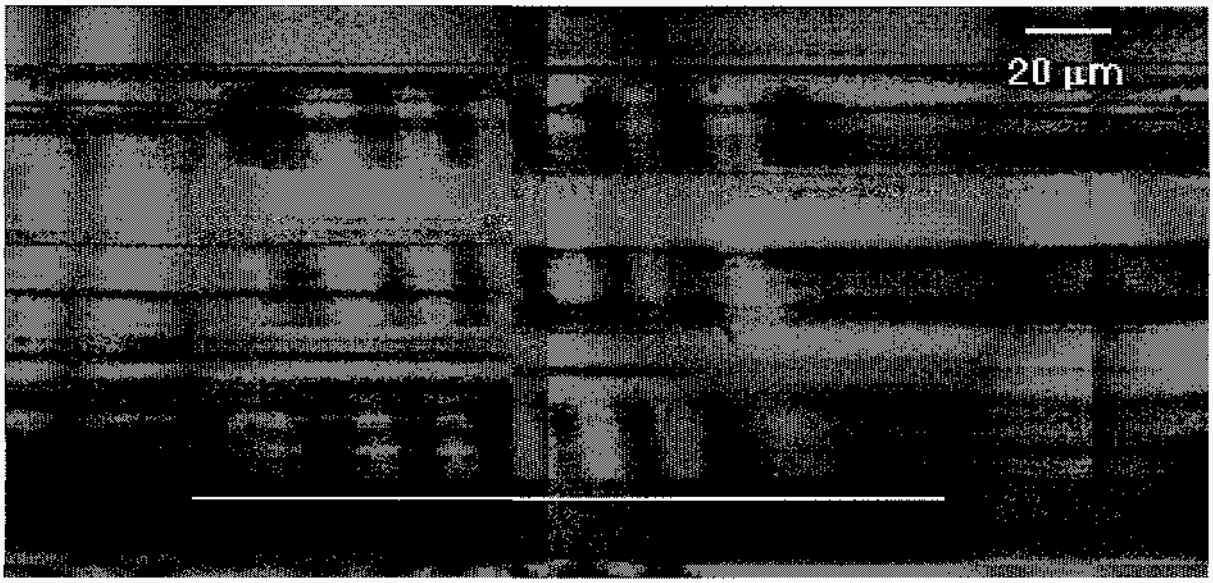
20 µm

Fig. 4a

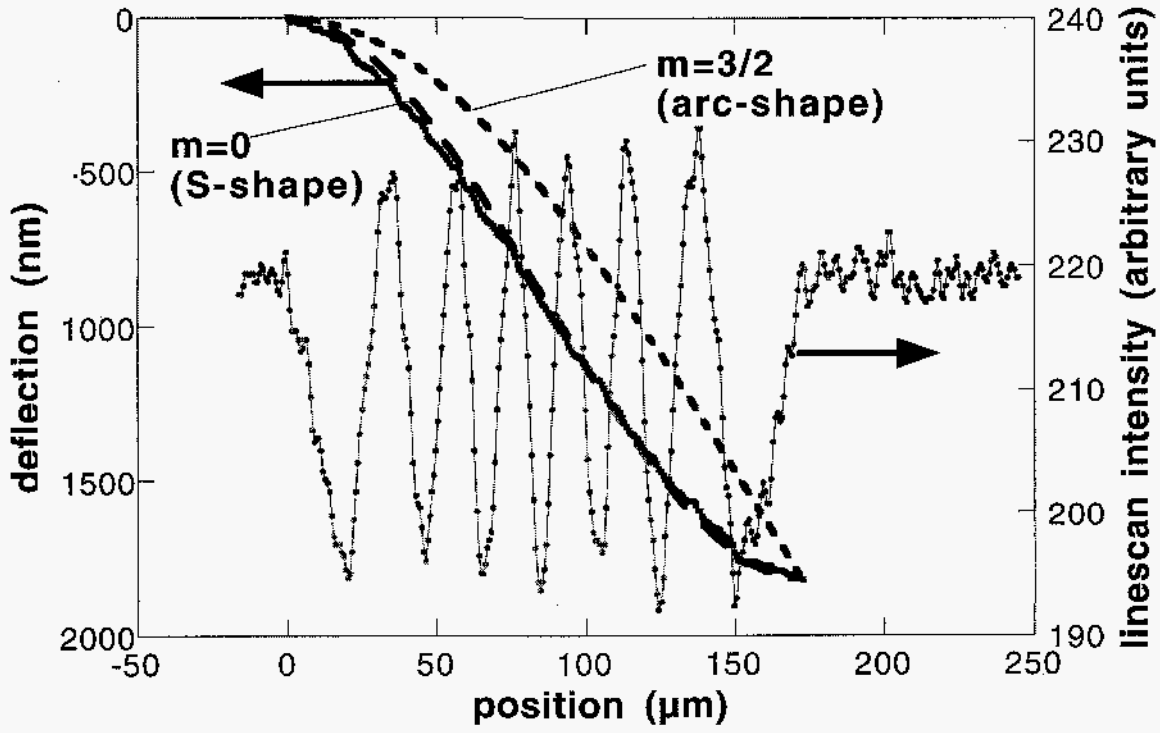
m=3/2
(arc-shape)
m=0
(S-shape)
deflection (nm)
linescan intensity (arbitrary units)
position (µm)
0
500
1000
1500
2000
240
230
220
210
200
190
-50
0
50
100
150
200
250

Fig. 4b

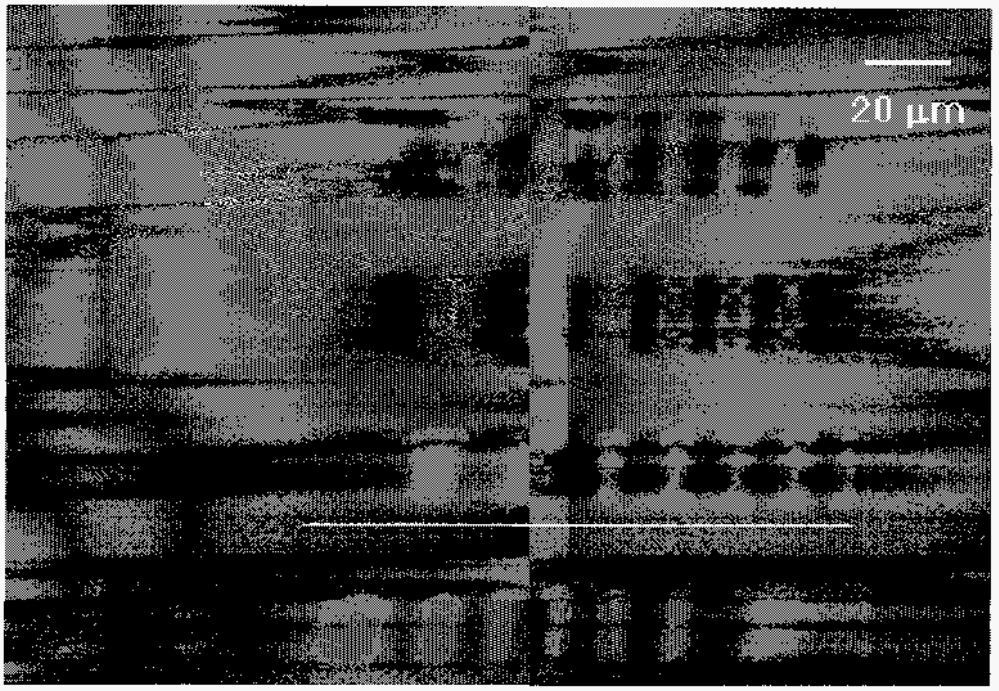
20 µm

Fig. 5a

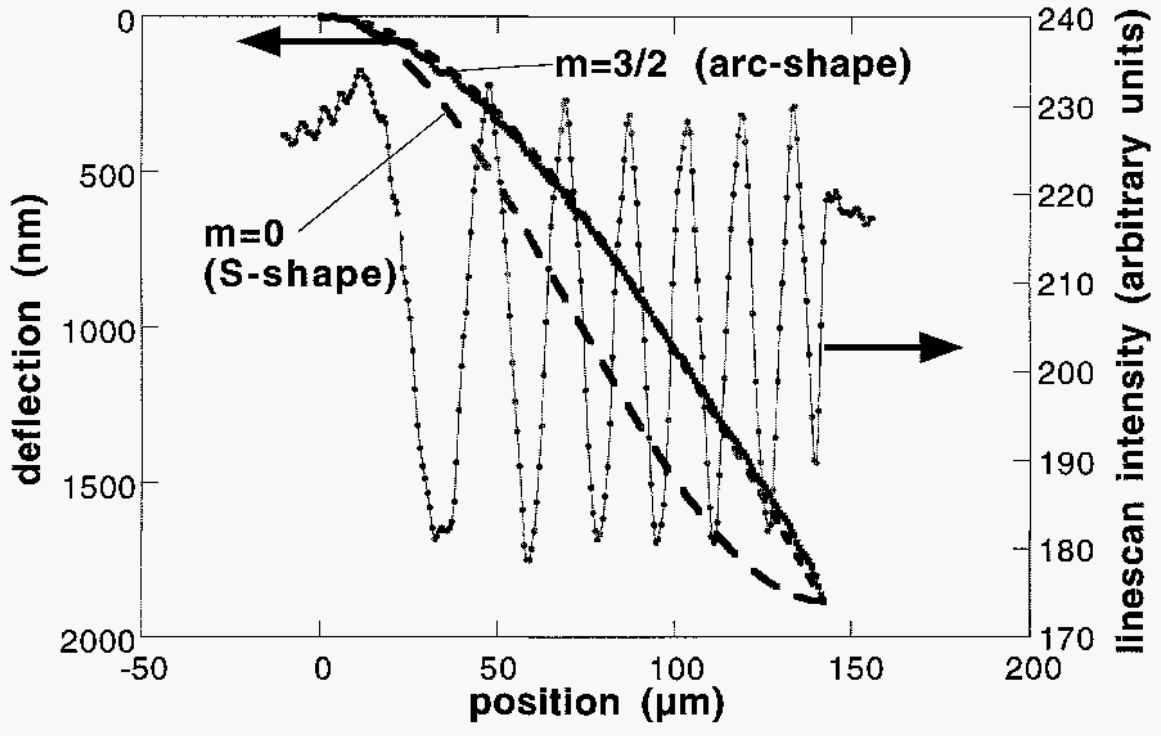
m=3/2 (arc-shape)
m=0
(S-shape)
deflection (nm)
linescan intensity (arbitrary units)
position (µm)
0
500
1000
1500
2000
240
230
220
210
200
190
180
170
-50
0
50
100
150
200

Fig. 5b

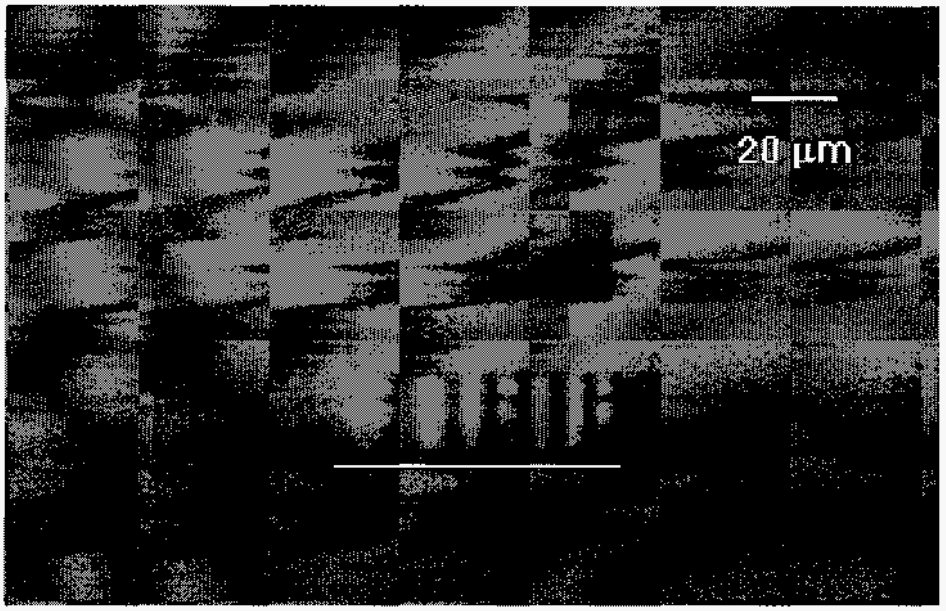
20 µm

Fig. 6a

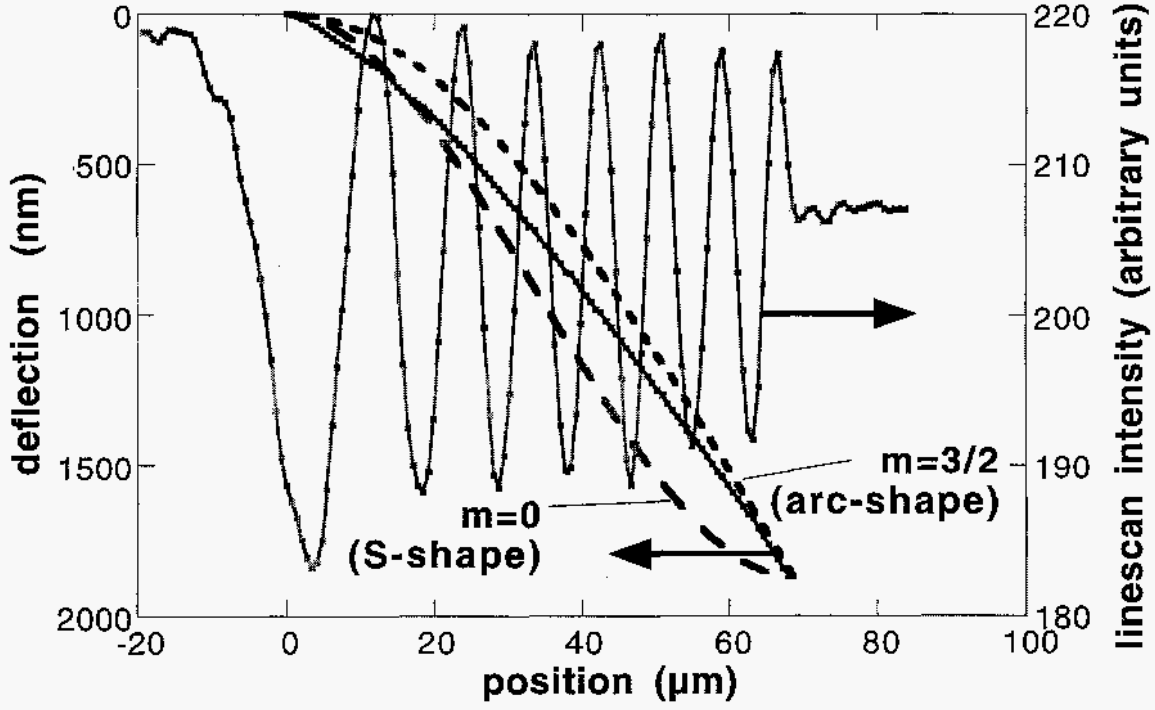
deflection (nm)
linescan intensity (arbitrary units)
position (µm)
m=0
(S-shape)
m=3/2
(arc-shape)
0
500
1000
1500
2000
220
210
200
190
180
-20
0
20
40
60
80
100

Fig. 6b

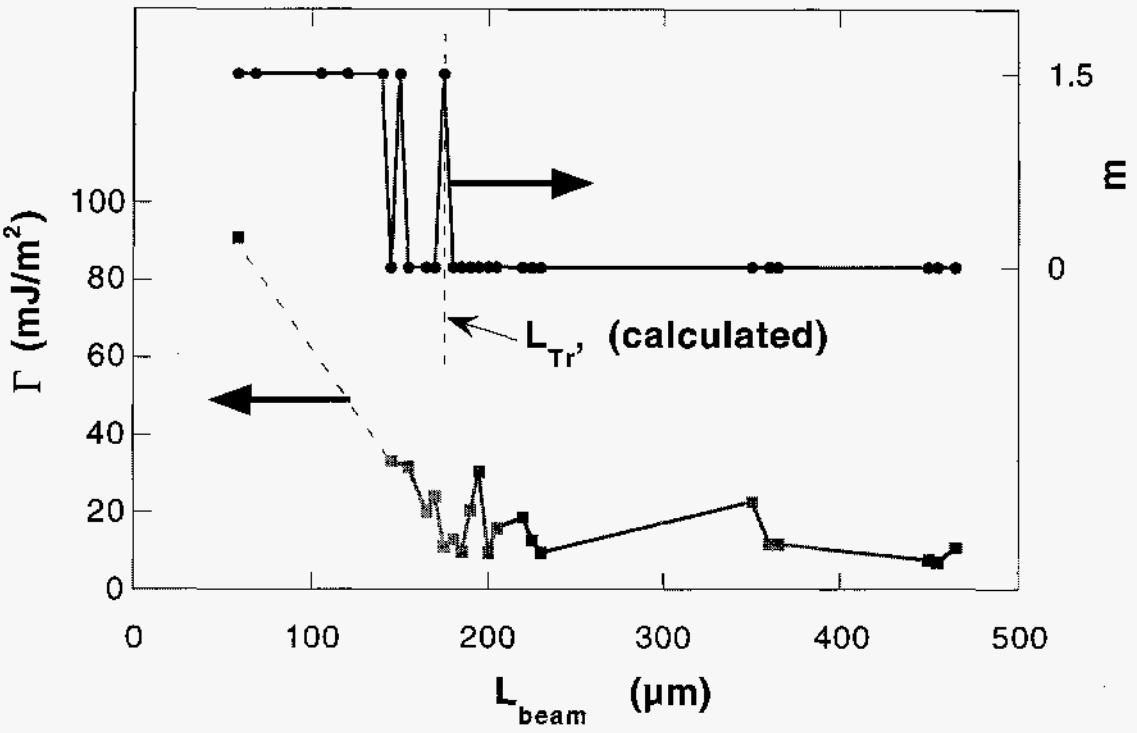
Γ (mJ/m²)
100
80
60
40
20
0
0
100
200
300
400
500
L_beam (μm)
1.5
m
0
L_Tr, (calculated)

Fig. 7a

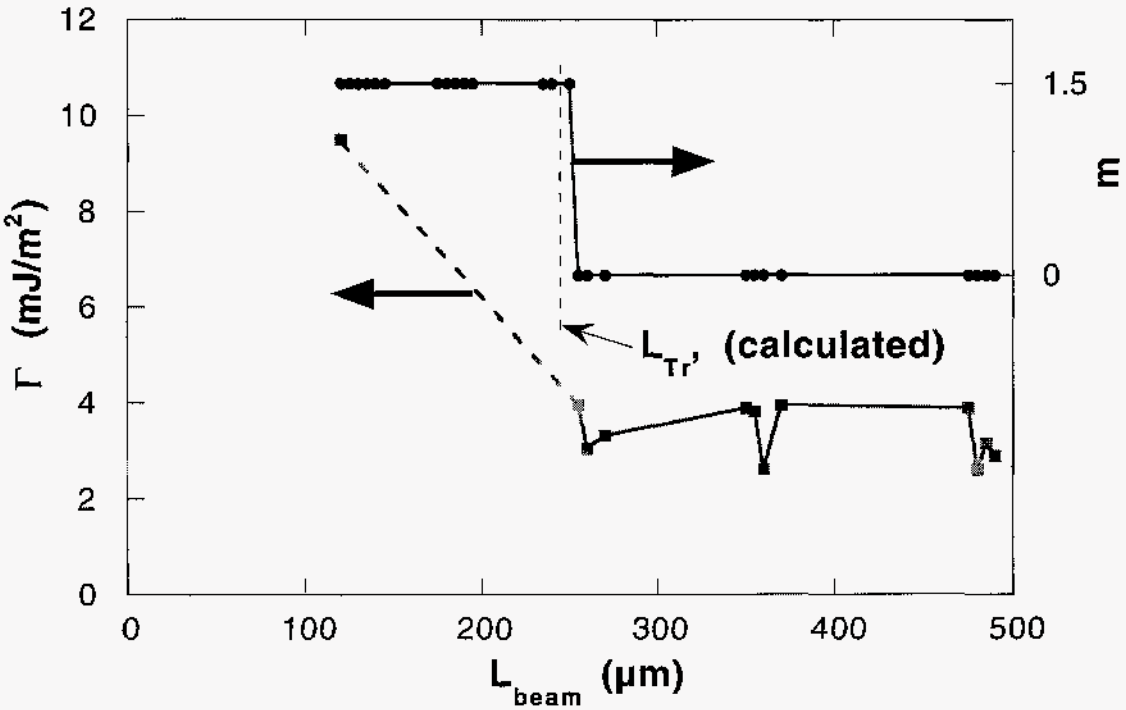
Γ (mJ/m²)
12
10
8
6
4
2
0
0
100
200
300
400
500
L_beam (μm)
1.5
m
0
L_Tr, (calculated)

Fig.7b

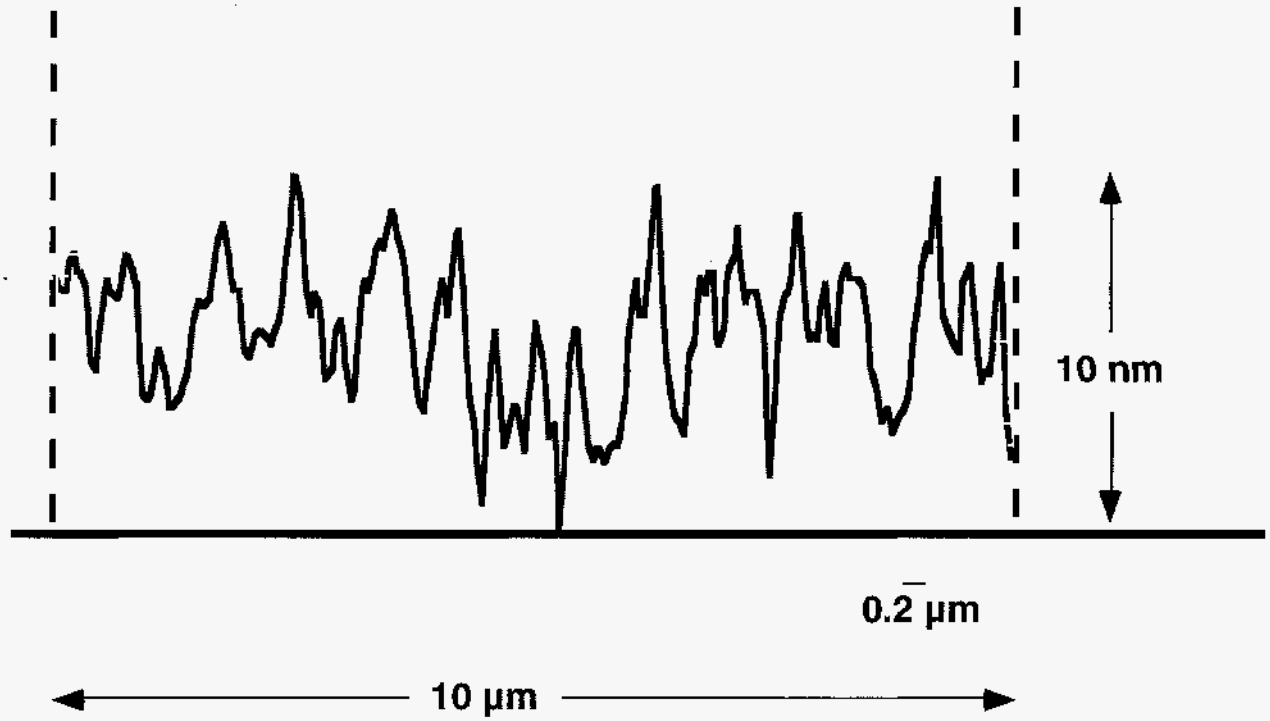

Fig. 8

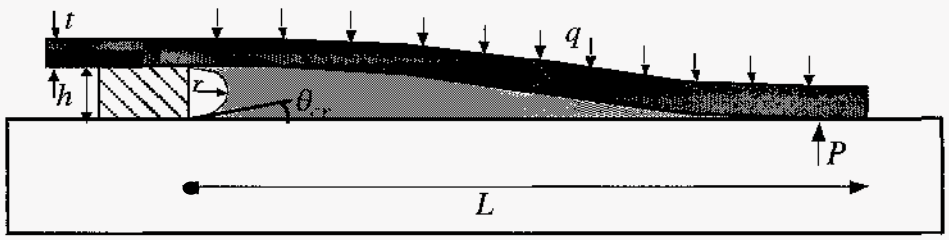

Fig. A1